

Modelling incomplete fusion dynamics of weakly-bound nuclei at near-barrier energies

Alexis Diaz-Torres

Department of Physics, Faculty of Engineering and Physical Sciences, University of Surrey, Guildford, Surrey GU2 7XH, United Kingdom

E-mail: a.diaztorres@surrey.ac.uk

Abstract. The classical dynamical model for reactions induced by weakly-bound nuclei at near-barrier energies is developed further. It allows a quantitative study of the role and importance of incomplete fusion dynamics in asymptotic observables, such as the population of high-spin states in reaction products as well as the angular distribution of direct alpha-production. Model calculations indicate that incomplete fusion is an effective mechanism for populating high-spin states, and its contribution to the direct alpha production yield diminishes with decreasing energy towards the Coulomb barrier. It also becomes notably separated in angles from the contribution of no-capture breakup events. This should facilitate the experimental disentanglement of these competing reaction processes.

PACS numbers: 25.60.Pj, 25.60.Gc, 25.60.-t, 24.10.-i

1. Introduction

Nuclear physics research has entered a new era with developments of radioactive nuclear beam facilities, where nuclear reactions are the primary probe of the new physics, such as novel structural changes. In those facilities, the low-energy nuclear reactions research is highly focused on understanding astrophysically important reaction rates involving exotic nuclei. These are often weakly-bound with a few-body, cluster structure that can easily be dissociated in their interaction with other nuclei. Understanding the breakup mechanism and its impact on nuclear reaction dynamics is essential. A major consequence of breakup is that a rich scenario of reaction pathways arises, such as events where (i) not all the resulting breakup fragments might be captured by the target, termed incomplete fusion (ICF), (ii) the entire projectile is captured by the target, called complete fusion (CF), and (iii) none of the breakup fragments are captured, termed no-capture breakup (NCBU).

Since the availability of intense exotic beams is still limited, extensive experimental research has recently been carried out exploiting intense beams of stable weakly-bound nuclei, such as ${}^6,7\text{Li}$ and ${}^9\text{Be}$ [1, 2]. Understanding the effect of their breakup on near-barrier fusion has been a key aspect of these investigations [3]. These have definitively

demonstrated that breakup suppresses the above-barrier fusion cross sections. Most recently, experimental activities have been focused on disentangling breakup and competing reaction mechanisms from inclusive and exclusive coincidence measurements [4, 5, 6, 7, 8]. One of the challenges is to obtain a complete quantitative understanding of the breakup mechanism and its relationship with near-barrier fusion. This research is guided by complete sub-barrier breakup measurements [9].

Theoretical works have addressed the low-energy reaction dynamics of weakly-bound nuclei using quantum mechanical, classical and mixed quantum-classical approaches [10, 11, 12, 13, 14, 15, 16, 17]. Among these, the continuum-discretised coupled channels (CDCC) framework has been very successful [10, 13, 16, 17]. However, existing quantum models have limitations [18], as they cannot calculate integrated ICF and CF cross sections unambiguously. Neither, after the formation of ICF products, can they follow the evolution of the surviving breakup fragment(s) since ICF results in depletion of the total few-body wave function.

These difficulties are overcome by the three-dimensional classical dynamical reaction model suggested in Ref. [19]. A crucial *input* of this model is a stochastically sampled breakup function proposed in Ref. [20], which can be determined from sub-barrier breakup measurements [9, 20]. This function encodes the effects of the Coulomb and nuclear interactions that cause the projectile breakup. Hence, this approach is *not* a breakup model, rather it is a quantitative dynamical model for relating the sub-barrier NCBU to the above-barrier ICF and CF of weakly-bound nuclei [20]. The model has been successfully applied to interpreting fusion measurements of weakly-bound nuclei [7, 9], and isomer ratio measurements [21].

In this paper, I report on further developments of this classical dynamical model. The key new aspect is the time propagation of the surviving breakup fragment and the ICF product, allowing the description of their asymptotic angular distribution and dynamical variables. These should be very useful in (i) current experimental activities aimed at disentangling competing reaction mechanisms from asymptotic observables such as alpha-production yields [8], (ii) interpreting particle- γ -coincidence experiments [22], and (iii) applications to γ ray spectroscopy [23, 24, 25]. The new developments are illustrated with a simplified test case that does *not* aim at adjusting any measurements. It is worth mentioning that various dynamical models have been proposed for multi-fragmentation and ICF in heavy-ion induced reactions at energies well-above the Coulomb barrier ($\gtrsim 10$ MeV/nucleon), as recently reviewed in Ref. [22]. In this different context, some of those models (e.g., Refs. [26, 27]) use concepts and techniques (e.g., classical trajectory, Monte Carlo sampling) that overlap with some involved in the present model. The model is explained in Section 2. In Section 3, numerical results are discussed, and a summary is given in Section 4.

2. Model

The main features of the model are as follows:

- (i) The target T is initially at rest in the origin of the laboratory frame, whilst the weakly-bound (two-body) projectile P approaches the target (along the z-axis) with incident energy E_0 and orbital angular momentum L_0 . For each L_0 (chosen to be an integer number of \hbar) an *ensemble* of N incident projectiles is considered. Including the $P - T$ mutual Coulomb and nuclear forces, classical equations of motion determine an orbit with a definite distance of closest approach $R_{min}(E_0, L_0)$.
- (ii) The complexity of the projectile dissociation is empirically encoded in a density of (local breakup) probability $\mathcal{P}_{BU}^L(R)$, a function of the projectile-target separation R , such that $\mathcal{P}_{BU}^L(R)dR$ is the probability of breakup in the interval R to $R + dR$ (see Appendix A). A key feature is that for a given projectile-target combination, both measurements [9, 20] and CDCC calculations [19] indicate that the integral of this breakup probability density along a given classical orbit is an exponential function of its distance of closest approach, $R_{min}(E_0, L_0)$:

$$P_{BU}(R_{min}) = 2 \int_{R_{min}}^{\infty} \mathcal{P}_{BU}^L(R)dR = A \exp(-\alpha R_{min}). \quad (1)$$

Consequently, $\mathcal{P}_{BU}^L(R)$ has the same exponential form, $\mathcal{P}_{BU}^L(R) \propto \exp(-\alpha R)$. (The factor of 2 highlights that breakup may occur along the entrance or exit branch of the trajectory, although the exponential form will clearly place maximum probability of breakup at R_{min} .) This function is sampled to determine the position of breakup in the orbit discussed in (i). In this position, the projectile is instantaneously broken up into fragments F1 and F2. These interact with T , and with each other, through real central two-body potentials having Coulomb barriers V_B^{ij} at separations R_B^{ij} , $i, j = 1, 2, T$, $i \neq j$.

- (iii) The instantaneous dynamical variables of the excited projectile at breakup, namely its total internal energy ε_{12} , its angular momentum $\vec{\ell}_{12}$ and the separation of the fragments \vec{d}_{12} are all Monte Carlo sampled. The initial separation d_{12} between the fragments and its orientation \vec{d}_{12} are determined by sampling the radial and angular probability distributions of the projectile ground-state (g.s.) wave function, respectively. For a two-body projectile with 0^+ g.s., a very good approximation for calculating d_{12} is through a Gaussian sampling function in the classically allowed region of the fragments, whilst the orientation of \vec{d}_{12} is isotropic. (This will be used in the test case below.) For high ℓ_{12} excitations, when there is no barrier between F1 and F2, d_{12} is equated with their external turning point. The orientation of $\vec{\ell}_{12}$ is chosen randomly from all directions orthogonal to \vec{d}_{12} . ℓ_{12} is sampled uniformly in the interval $[0, \ell_{max}]$, whilst for ε_{12} an exponentially decreasing function for energies between the top of the barrier (V_B^{12}) and a chosen maximum ε_{max} is sampled. Both ℓ_{max} and ε_{max} are increased until convergence of the observables occur.
- (iv) Having fixed the position and dynamical variables of the excited projectile fragments at the moment of breakup, the instantaneous velocity of the particles F1, F2 and T is determined by conservation of energy, linear momentum and angular momentum in the overall center-of-mass frame (see Appendix B). These breakup

initial conditions are transformed to the laboratory frame where the three bodies are propagated in time. The calculated trajectories of F1, F2 and T determine the number of ICF, CF and NCBU events, fragment Fj being assumed to be captured if the classical trajectories take it within the fragment-target barrier radius R_B^{jT} .

- (v) From the N breakup events sampled for each projectile angular momentum L_0 , the numbers of events N_i in which $i = 0$ (NCBU), 1 (ICF), or 2 (CF) fragments are captured determine the relative yields $\widetilde{P}_i = N_i/N$ of these three reaction processes after breakup, with $\widetilde{P}_0 + \widetilde{P}_1 + \widetilde{P}_2 = 1$. The absolute probabilities $P_i(E_0, L_0)$ of these processes are expressed in terms of the relative yields and the integrated breakup probability over the whole trajectory $P_{BU}(R_{min})$:

$$P_0(E_0, L_0) = P_{BU}(R_{min}) \widetilde{P}_0, \quad (2)$$

$$P_1(E_0, L_0) = P_{BU}(R_{min}) \widetilde{P}_1, \quad (3)$$

$$P_2(E_0, L_0) = [1 - P_{BU}(R_{min})] H(L_{cr} - L_0) + P_{BU}(R_{min}) \widetilde{P}_2, \quad (4)$$

where $H(x)$ is the Heaviside step function and L_{cr} is the critical partial wave for projectile fusion. The cross sections are calculated using

$$\sigma_i(E_0) = \pi \lambda^2 \sum_{L_0} (2L_0 + 1) P_i(E_0, L_0), \quad (5)$$

where $\lambda^2 = \hbar^2/[2m_P E_0]$ and m_P is the projectile mass.

Beside the absolute cross sections (5), asymptotic observables, such as the angle, kinetic energy and relative energy distributions of the fragments from NCBU events, are calculated by tracking their trajectories to a large distance from the target.

- (vi) For the ICF events, the time propagation of the ICF product and the surviving breakup fragment is now incorporated into this model as follows. The fragment Fj (after overcoming the Coulomb barrier V_B^{jT}) reaches the target radius, forming the ICF product, while the other fragment flies away. At this moment, the three-body propagation turns into a two-body propagation, with definite interaction potentials and initial conditions. These are determined by the position and velocity of the three particles, at the moment when the ICF product is formed. These also yield the spin and excitation energy distributions of the *primary* ICF product. The asymptotic angular distribution of the ICF product and the surviving breakup fragment is calculated in terms of their trajectories.

3. Numerical results

This model is implemented in the PLATYPUS code, as described in Ref. [28]. In order to illustrate the new developments of (vi), calculations are carried out at a laboratory energy of $E_0 = 45$ and 65 MeV, for the reaction of a pseudo- ^8Be projectile P (modeled as a weakly-bound s -state of two α -particles [19]) with the ^{208}Pb target T .

The breakup function $P_{BU}(R_{min})$ in eq. (1) has parameters $A = 5.98 \times 10^3$ and $\alpha = 0.85 \text{ fm}^{-1}$, which was deduced in Ref. [19] from mapping fusion measurements for

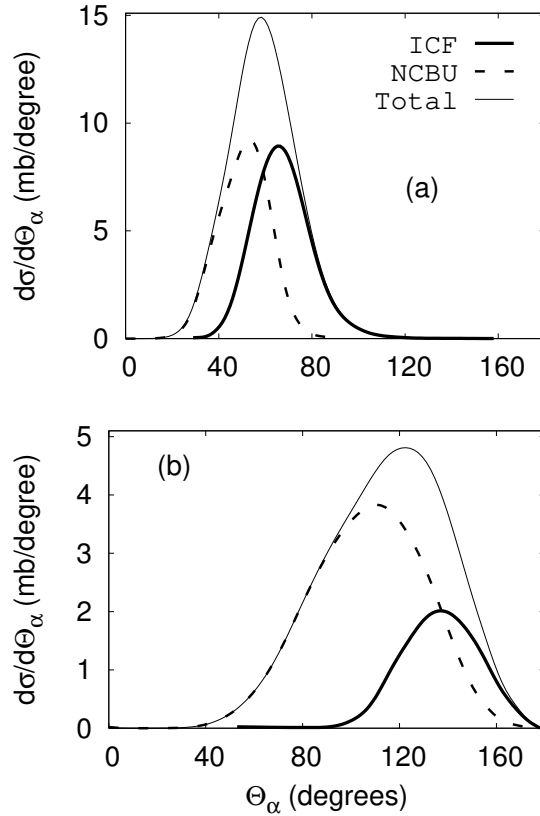


Figure 1. Angular distribution of direct alpha-production for ${}^8\text{Be} + {}^{208}\text{Pb}$ at two laboratory energies E_0 : (a) 65 MeV, and (b) 45 MeV. With decreasing energy towards the Coulomb barrier, the NCBU events dominate, separating its centroid substantially from that of the ICF events. The total alpha-production distribution changes its shape notably.

the ${}^9\text{Be} + {}^{208}\text{Pb}$ system with this test reaction. This is because the model is limited to solving a three-body problem. However, very recent measurements [9] have shown that prompt ${}^9\text{Be}$ breakup occurs dominantly through an excited ${}^8\text{Be}$ nucleus, validating the approximation of a ${}^9\text{Be}$ projectile by ${}^8\text{Be}$.

The nuclear interaction between the alpha particle and the ICF product ${}^{212}\text{Po}$ is considered to be the Woods-Saxon potential $(V, r, a) \equiv (33.98 \text{ MeV}, 1.48 \text{ fm}, 0.63 \text{ fm})$ resulted from the global Broglia-Winther parametrization [29]. (Please note that in the potential the radius parameter is multiplied by $A_T^{1/3}$.) The rest of the model parameters are the same as in Ref. [19].

Figure 1 shows the angular distribution of direct alpha-production for two laboratory energies near the $P - T$ s-wave Coulomb barrier (39.9 MeV), namely (a) $E_0 = 65$, and (b) 45 MeV. The contribution of the ICF and NCBU events is represented by thick solid and thick dashed lines, respectively. Their incoherent sum is represented by the thin solid line. Its shape significantly changes as the incident energy decreases. While the contribution of the ICF and NCBU events appears to be similar at well-above

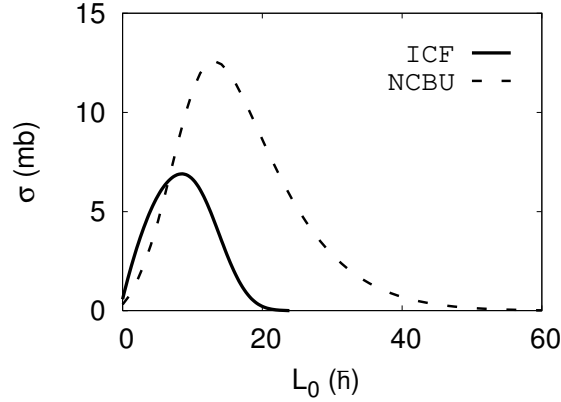


Figure 2. ICF and NCBU cross sections as a function of the relative angular momenta L_0 for ${}^8\text{Be} + {}^{208}\text{Pb}$ at $E_0 = 45$ MeV. The contribution of high-partial waves shifts the NCBU distributions in Fig. 1 to smaller angles, with respect to the ICF distributions.

barrier energies [panel (a)], the NCBU contribution gradually dominates with decreasing energy towards the barrier [panel (b)]. Here, its centroid significantly separates from the centroid of the ICF contribution. Both centroids shift to higher angles as the incident energy decreases, due to the reduction of relative partial waves affecting these reaction processes. However, the NCBU centroid always remains lower than the ICF centroid, as expected. This is because higher partial waves contribute to the NCBU process (see Fig. 2). Fig. 2 presents the incident angular momentum distribution of the ICF (solid line) and NCBU (dashed line) processes at a laboratory energy of $E_0 = 45$ MeV.

Figure 3 shows the angular momentum distribution of *primary* ICF (${}^{212}\text{Po}$) and CF (${}^{216}\text{Rn}$) products at (a) $E_0 = 65$, and (b) 45 MeV. The ICF spin distribution is represented in terms of both the ${}^8\text{Be}$ incident angular momentum L_0 (thick solid line) and the angular momentum brought in by the α -particle into the ${}^{208}\text{Pb}$ target (thin solid line). These representations result in two very different ICF angular momentum distributions, both providing relevant features of the ICF dynamics as explained below.

Comparing the thick solid line with the CF spin distribution (dashed line) it is seen that the localization of the L_0 -window for ICF significantly depends on the incident energy E_0 . Their overlap strongly increases as E_0 decreases towards the barrier [panel (b)], indicating that ICF and CF are two competing reaction processes at near-barrier energies. However, CF following ${}^8\text{Be}$ breakup is here a very small component (1.5%) of the CF cross section (149.2 mb). Instead, either one of the α -particles is captured by the target, contributing to the ICF cross section (84.7 mb), or the two α -particles survive and contribute to the NCBU cross section (238.8 mb). At $E_0 = 65$ [panel (a)], CF following ${}^8\text{Be}$ breakup is very substantial, representing 41% of the CF cross section (981.5 mb). This significantly shifts down the maximum of the CF spin distribution (dashed line) with respect to the critical angular momentum L_{cr} for ${}^8\text{Be}$ fusion as an inert projectile (thick arrow). Here, L_0 values around L_{cr} determine the ICF cross section (273.6 mb) which is similar to the NCBU cross section (259.3 mb).

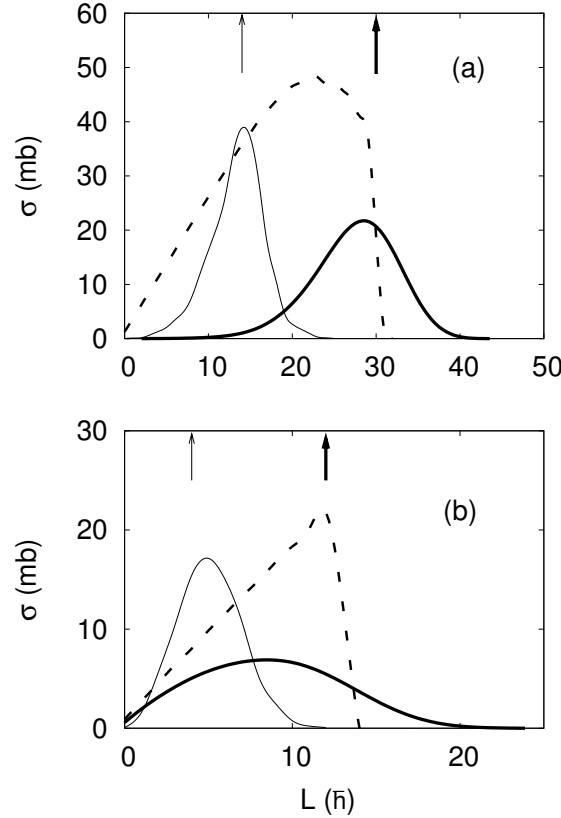


Figure 3. Spin distribution of *primary* fusion products resulting from the ${}^8\text{Be} + {}^{208}\text{Pb}$ reaction at two laboratory energies E_0 : (a) 65 MeV, and (b) 45 MeV. The CF (${}^{216}\text{Rn}$) spin distribution is presented by the dashed line, whilst the ICF (${}^{212}\text{Po}$) spin distribution is shown in two representations, *i.e.*, in terms of (i) the ${}^8\text{Be}$ incident angular momentum L_0 (thick solid line), and (ii) the angular momentum brought in by the α -particle into the ${}^{208}\text{Pb}$ target (thin solid line). The thick arrow denotes L_{cr} for ${}^8\text{Be}$ fusion as an inert projectile, whereas the thin arrow is l_{cr} for fusion of a direct beam of α -particles (with half of E_0) on ${}^{208}\text{Pb}$. The relevant features are: (1) the ICF mechanism increases the angular momentum brought in by the α -particle into ${}^{208}\text{Pb}$ (thin solid line goes beyond the thin arrow), (2) the relative localization of the L_0 -window for CF and ICF significantly depends on E_0 (dashed and thick solid lines), strongly overlapping as E_0 decreases, and (3) CF following ${}^8\text{Be}$ breakup becomes substantial with increasing E_0 , shifting down the maximum of the CF spin distribution (dashed line) with respect to the thick arrow.

The ICF spin distributions (thin solid line) in Fig. 3 are the crucial ones in order to access the effectiveness of the ICF mechanism for populating high-spin states in ${}^{212}\text{Po}$. It is observed that the tail of these distributions goes well beyond the thin arrow which denotes l_{cr} for fusion, on the ${}^{208}\text{Pb}$ target, of a direct beam of α -particles with half of E_0 . Clearly, the extra torque caused by the interaction between the fusing and surviving α -particles enhances the angular momentum of the ICF product. This interaction also affects the excitation energy of ${}^{212}\text{Po}$ substantially, as presented in Fig. 4.

Fig. 4 shows the excitation energy distribution of the *primary* ICF product ${}^{212}\text{Po}$

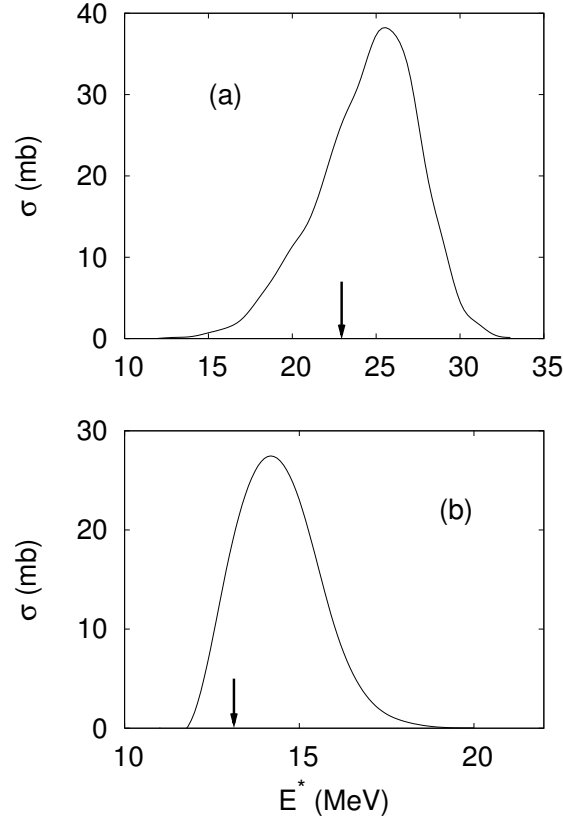


Figure 4. Excitation energy distribution of the *primary* ICF product ^{212}Po resulting from the $^8\text{Be} + ^{208}\text{Pb}$ reaction at two laboratory energies E_0 : (a) 65 MeV, and (b) 45 MeV. The arrow denotes the excitation energy of ^{212}Po , when this compound nucleus is formed by fusion of a direct beam of α -particles, with half of E_0 , on ^{208}Pb . Following breakup of ^8Be , the fusing α -particle is significantly affected by the interaction with the surviving α -particle. This spreads the ^{212}Po excitation energy over a range of values. The distribution becomes narrower and its maximum approaches the arrow, as E_0 decreases towards the barrier.

(thin solid line) at (a) $E_0 = 65$, and (b) 45 MeV. It is caused by the interaction between the fusing and surviving α -particles during the ICF process. The arrow corresponds to the pre-determined excitation energy of ^{212}Po , when this nucleus is formed through CF of a direct beam of α -particles (with half of E_0) on ^{208}Pb . This value remains smaller (by a few MeV) than the excitation energy associated with the maximum of the distribution. The shape of the distribution also changes with E_0 , becoming narrower as E_0 decreases towards the barrier. These distributions along with the ICF spin distributions in Fig. 3 (thin solid line) are vital for a reliable prediction of the yield of final ICF products. To my knowledge, these aspects have not been yet included in broadly used evaporation codes which mostly describe CF evaporation residues.

The present model can be applied to more realistic cases (e.g., ^{11}Be induced reactions), provided all the necessary information for Monte Carlo sampling is known (e.g., the breakup function and the projectile g.s. wave-function). When one of the

breakup fragments is neutral, its capture by the target nucleus can be assumed to occur when its trajectory takes it within the target radius. Although not implemented yet, the model can also predict the elastic angular distribution of the projectile. This distribution can easily be calculated in terms of the projectile-target orbits and the probability of the weakly-bound projectile's survival (see Appendix A), i.e., this probability weighting the contribution of the different projectile-target orbits. Direct reaction processes other than the elastic breakup may significantly contribute to observables associated with NCBU, CF and ICF. These are not included in the model yet. However, their contributions could be included using transfer and inelastic-breakup functions. Of course, these would make the calculations more complex, as these direct reaction processes result in additional bifurcation points along the projectile-target orbits. Nevertheless, their inclusion as well as the treatment of more complex projectiles (e.g., ${}^6\text{He}$ and ${}^{11}\text{Li}$) will be interesting, necessary developments of the present approach.

4. Summary

The classical dynamical model for reactions of weakly-bound nuclei at near-barrier energies has been developed further. It allows us to quantify the role and importance of ICF dynamics in asymptotic reaction observables, such as the angular distribution of the direct alpha-production. The ICF contribution to this yield diminishes with decreasing energy towards the barrier. However, the ICF and NCBU contributions are clearly separated in angles at near-barrier energies, facilitating the experimental disentanglement of these competing reaction processes. The present developments also provide the spin and excitation energy distributions of primary ICF products, which are essential ingredients for calculating the yield of final ICF products with present evaporation codes. The ICF mechanism appears to be an effective route for producing high-spin states. All these observables may also be affected by other direct processes, such as transfer [30], which are not included in the model yet. Nevertheless, the present classical dynamical model is a powerful tool for interpreting fusion measurements involving radioactive nuclei and in applications to γ ray spectroscopy. The development of a unified quantum dynamical description of relevant reaction processes (ICF, CF, NCBU and transfer) remains a great theoretical challenge. One possibility of tackling this issue could be through a time-dependent density-matrix approach incorporating the concept of quantum decoherence [18, 31].

Acknowledgments

The author thanks B. Bayman and M. Dasgupta for suggesting Appendix A, and J.A. Tostevin for discussions related to Appendix B. Support from the UK Science and Technology Facilities Council (STFC) Grant No. ST/F012012/1 is acknowledged.

Appendix A. Breakup probability function

Let us define two probabilities: (i) the probability of breakup between R and $R + dR$, $\rho(R)dR$ [being $\rho(R)$ a density of probability], and (ii) the probability of the weakly-bound projectile's survival from ∞ to R , $S(R)$. The survival probability at $R + dR$, $S(R + dR)$, can be written as follows

$$S(R + dR) = S(R) [1 - \rho(R)dR]. \quad (\text{A.1})$$

Expression (A.1) suggests the following differential equation for the survival probability $S(R)$,

$$\frac{dS(R)}{dR} = -S(R) \rho(R), \quad (\text{A.2})$$

whose solution is [$S(\infty) = 1$]:

$$S(R) = \exp\left(-\int_{\infty}^R \rho(R)dR\right). \quad (\text{A.3})$$

From (A.3), the breakup probability at R , $B(R) = 1 - S(R)$. If $\int_{\infty}^R \rho(R)dR \ll 1$, $B(R)$ can be written as

$$B(R) \approx \int_{\infty}^R \rho(R)dR. \quad (\text{A.4})$$

From (A.4), identifying $\rho(R)$ with $\mathcal{P}_{BU}^L(R)$, we obtain expression (1) for the breakup probability integrated along a given classical orbit.

Appendix B. Matching prior- and post-breakup stages

The integrals of motion in the overall center-of-mass (CM) system are the total energy $E_{tot} = \frac{m_T}{(m_T + m_P)} E_0$, the total linear momentum $\vec{P}_{tot} = \vec{0}$, and the total angular momentum $\vec{L}_{tot} = m_P b_0 (\vec{v} - \vec{V}_{CM})$ that is orthogonal to the initial reaction plane. m_T , m_P , b_0 , \vec{v} , and \vec{V}_{CM} are the mass of the target and projectile, the impact parameter between the projectile and the target, the velocity of the incident projectile in the laboratory system and the CM velocity, respectively.

Just after breakup, the two-body projectile is excited to a definite state (ε_{12} , $\vec{\ell}_{12}$ and \vec{d}_{12}), as explained in Section 2. The relative vector between P and T (\vec{R}_{PT}) is also known. Thus, the separation between the three bodies is known. The modulus of the velocity between P and T ($V_{PT} = P_{PT}/\mu_{PT}$) results from the total energy conservation

$$E_{tot} = \varepsilon_{12} + U_{1T}(r_{1T}) + U_{2T}(r_{2T}) + P_{PT}^2/2\mu_{PT}, \quad (\text{B.1})$$

where U is the interaction potential between the target and the breakup fragments.

The total linear momentum $\vec{P}_{tot} = \vec{p}_T + \vec{p}_1 + \vec{p}_2 = \vec{p}_T + \vec{p}_{P^*}$, where \vec{p}_{P^*} is the momentum of the center of mass of excited P relative to the overall CM. We need the velocities of P and T relative to the overall CM (\vec{v}_P and \vec{v}_T) to complete the initial

conditions for subsequent propagation in time of the three bodies. These velocities are related to each other by the expressions

$$\vec{v}_T = -\frac{m_P}{m_T} \vec{v}_P, \quad (\text{B.2})$$

$$\vec{V}_{PT} = \vec{v}_P - \vec{v}_T, \quad (\text{B.3})$$

where the magnitude of \vec{V}_{PT} is known through expression (B.1). To know the direction of this velocity the conservation of total angular momentum is applied.

The total angular momentum $\vec{L}_{tot} = \vec{\ell}_{12} + \vec{L}_{PT}$, so the angular momentum (\vec{L}_{PT}) associated with relative motion of P and T about CM is known. This vector can be written as

$$\vec{L}_{PT} = m_P \vec{R}_{PT} \times \vec{v}_P. \quad (\text{B.4})$$

We now write \vec{v}_P in terms of radial and transverse components as follows:

$$\vec{v}_P = \tilde{v}_P^{(r)} \vec{r} + \tilde{v}_P^{(q)} \vec{q}, \quad (\text{B.5})$$

where $\vec{r} = \vec{R}_{PT}/R_{PT}$ and $\vec{q} = \vec{n} \times \vec{r}$, being $\vec{n} = \vec{L}_{PT}/L_{PT}$. The transverse component $\tilde{v}_P^{(q)} = L_{PT}/(m_P R_{PT})$, and for the target $\tilde{v}_T^{(q)} = -L_{PT}/(m_T R_{PT})$. The radial component is obtained using expressions (B.2)-(B.3) and knowing the transverse component:

$$\tilde{v}_P^{(r)} = \pm \left\{ V_{PT}^2 - \left[\tilde{v}_P^{(q)} \left(1 + \frac{m_P}{m_T} \right) \right]^2 \right\}^{1/2} / \left(1 + \frac{m_P}{m_T} \right). \quad (\text{B.6})$$

Both positive and negative roots are consistent with the conservation of the integrals of motion. Hence, both roots are uniformly sampled. Finally, the position and velocity vectors of the projectile fragments and the target are transformed to the laboratory system using Galilean transformations.

References

- [1] Dasgupta M et al. 1999 *Phys. Rev. Lett.* **82** 1395, 2004 *Phys. Rev. C* **70** 024606
- [2] Beck C et al. 2003 *Phys. Rev. C* **67** 054602, 2010 *Nucl. Phys. A* **834** 440c
- [3] Canto L F et al. 2006 *Phys. Rep.* **424** 1, and references therein
- [4] Signorini C et al. 2003 *Phys. Rev. C* **67** 044607
- [5] Shrivastava A et al. 2006 *Phys. Lett. B* **633** 463
- [6] Beck C 2007 *Nucl. Phys. A* **787** 251c
- [7] Santra S et al. 2009 *Phys. Lett. B* **677** 139
- [8] Souza F A et al. 2009 *Nucl. Phys. A* **821** 36, 2010 *Nucl. Phys. A* **834** 420c
- [9] Rafiei R et al. 2010 *Phys. Rev. C* **81** 024601
- [10] Tostevin J A et al. 2001 *Phys. Rev. C* **63** 024617
- [11] Diaz-Torres A and Thompson I J 2002 *Phys. Rev. C* **65** 024606, and references therein
- [12] Diaz-Torres A et al. 2002 *Nucl. Phys. A* **703** 83
- [13] Diaz-Torres A et al. 2003 *Phys. Rev. C* **68** 044607
- [14] Yabana K et al. 2004 *Nucl. Phys. A* **738** 303c
- [15] Hagino K et al. 2004 *Nucl. Phys. A* **738** 475c
- [16] Beck C et al. 2007 *Phys. Rev. C* **75** 054605
- [17] Hashimoto S et al. 2009 *Prog. Theor. Phys.* **122** 1291
- [18] Thompson I J and Diaz-Torres A 2004 *Prog. Theor. Phys. Suppl.* **154** 69

- [19] Diaz-Torres A et al. 2007 *Phys. Rev. Lett.* **98** 152701
- [20] Hinde D J et al. 2002 *Phys. Rev. Lett.* **89** 272701
- [21] Gasques L R et al. 2006 *Phys. Rev. C* **74** 064615
- [22] Singh P P et al., 2009 *Phys. Lett. B* **671** 20, 2009 *Phys. Rev C* **80** 064603
- [23] Dracoulis G D et al. 1997 *J. Phys. G* **23** 1191
- [24] Mullins S M et al. 1997 *Phys. Lett. B* **393** 279, 1998 *Phys. Rev C* **58** 831, 2000 *Phys. Rev. C* **61** 044315
- [25] A. Jungclaus et al. 2002 *Phys. Rev. C* **66** 014312, 2003 *Phys. Rev. C* **67** 034302
- [26] K. Möhring et al 1988 *Phys. Lett. B* **203** 210
- [27] Bondorf J P et al 1992 *Phys. Rev. C* **46** 374
- [28] Diaz-Torres A 2007 PLATYPUS: a code for fusion and breakup in reactions induced by weakly-bound nuclei within a classical trajectory model with stochastic breakup *Preprint nucl-th/0712.2275*
- [29] Reisdorf W 1994 *J. Phys. G* **20** 1297
- [30] Diaz-Torres A et al. 2002 *Phys. Lett. B* **533** 265
- [31] Diaz-Torres A et al. 2008 *Phys. Rev. C* **78** 064604